

# Neural Network Surrogate Models for Absorptivity and Emissivity Spectra of Multiple Elements

Michael D. Vander Wal<sup>c</sup>, Ryan G. McClarren<sup>c</sup>, Kelli D. Humbird<sup>d</sup>

<sup>a</sup>*University of Notre Dame - Department of Aerospace and Mechanical Engineering  
University of Notre Dame Notre Dame Indiana USA 46556*

<sup>b</sup>*Lawrence Livermore National Laboratory 7000 East Ave Livermore California USA*

---

## Abstract

Simulations of high energy density physics are expensive in terms of computational resources. In particular, the computation of opacities of plasmas, which are needed to accurately compute radiation transport in the non-local thermal equilibrium (NLTE) regime, are expensive to the point of easily requiring multiple times the sum-total compute time of all other components of the simulation. As such, there is great interest in finding ways to accelerate NLTE computations. Previous work has demonstrated that a combination of fully-connected autoencoders and a deep jointly-informed neural network (DJINN) can successfully replace the standard NLTE calculations for the opacity of krypton. This work expands this idea to multiple elements in demonstrating that individual surrogate models can be also be generated for other elements with the focus being on creating autoencoders that can accurately encode and decode the absorptivity and emissivity spectra. Furthermore, this work shows that multiple elements across a large range of

---

*Email addresses:* [mvander5@nd.edu](mailto:mvander5@nd.edu) (Michael D. Vander Wal), [rmcclarr@nd.edu](mailto:rmcclarr@nd.edu) (Ryan G. McClarren), [humbird1@llnl.gov](mailto:humbird1@llnl.gov) (Kelli D. Humbird)

atomic numbers can be combined into a single autoencoder when using a convolutional autoencoder while maintaining accuracy that is comparable to individual fully-connected autoencoders. Lastly, it is demonstrated that DJINN can effectively learn the latent space of a convolutional autoencoder that can encode multiple elements allowing the combination to effectively function as a surrogate model.

*Keywords:* convolutional, autoencoder, spectra, absorption, absorptivity, emissivity, DJINN, Deep Jointly Informed Neural Network, surrogate, CRETIN, NLTE, non-local thermal equilibrium

---

# Neural Network Surrogate Models for Absorptivity and Emissivity Spectra of Multiple Elements

Michael D. Vander Wal<sup>c</sup>, Ryan G. McClarren<sup>c</sup>, Kelli D. Humbird<sup>d</sup>

<sup>c</sup>*University of Notre Dame - Department of Aerospace and Mechanical Engineering  
University of Notre Dame Notre Dame Indiana USA 46556*

<sup>d</sup>*Lawrence Livermore National Laboratory 7000 East Ave Livermore California USA*

---

## 1. Introduction

Nuclear fusion has been called the "Holy Grail"[1] of energy [2] due to the seemingly limitless amount of energy that controlled nuclear fusion could make available. Over the preceding decades there has been much investment into various different methods to try achieve this milestone. One of these methods is inertial confinement fusion (ICF). The National Ignition Facility (NIF) at Lawrence Livermore National Laboratory (LLNL) hosts many of the ICF experiments. The experiments are quite expensive, on the order of \$1+ million dollars per experiment. This great expense means that simulation is an integral part of the experiment design and selection process.

ICF experiments and simulations at NIF involve the firing of many lasers at a small target: often with the goal of trying to break even between the energy put into the fuel capsule and the energy liberated via nuclear fusion. The ultimate goal is to get closer to ignition which is the point at the energy liberated via nuclear fusion is enough to sustain continued nuclear fusion.

---

*Email addresses:* mvander5@nd.edu (Michael D. Vander Wal), rmclarr@nd.edu (Ryan G. McClarren), humbird1@llnl.gov (Kelli D. Humbird)

In these experiments, the lasers superheat and subsequently ablate a hollow, cylinder-like object made of gold called a hohlraum. Inside the hohlraum there is also a microcapsule of the fuel, a deuterium-tritium ice encased in a material such as beryllium or high-density carbon [3], intended to undergo fusion after being irradiated by x-rays emitted during the superheating and ablation of the hohlraum. The superheating of the hohlraum leads to the emission of x-rays which then heat and compress the microcapsule which results in varying levels of fusion occurring.

In these simulations, atomic physics are of particular importance. The atomic physics account for the various electronic transitions of atoms of the various elements involved. These electronic transitions and ionizations are important because they are what give rise to the spectral lines and broadband radiation that characterize the absorptivities and emissivities of these elements. These are in turn necessary for energy transfer calculations.

The accounting for the electron transitions leads to the usage of either local thermal equilibrium (LTE) or non-local thermal equilibrium (NLTE) physics. That is, it is largely an accounting for how many atoms have an electron that moves up or down in the atoms' energy levels as well as electrons that become free electrons or captured electrons [4, 5, 6]. The following processes are typically included in NLTE calculations:

- electron-impact excitation and de-excitation
- electron-impact ionization and three-body recombination
- photo-excitation and de-excitation
- photo-ionization and radiative recombination



- Bremsstrahlung and inverse-Bremsstrahlung
- scattering

The above list is not exhaustive. There are other processes that occur at very high energies (greater than 1 MeV) as well as nuclear conversion processes that affect ionization levels and electron populations [7].

LTE uses Kirchoff's Law to assume that absorptivity and emissivity are equal and is only characterized by temperature and makes look-up tables straightforward to implement. In contrast to LTE physics, temperature, density, and the radiative field characterize NLTE physics processes. In addition, the forward and backward processes are not equal in rate. This means that the counting of states and the subsequent solving of rate equations must be performed.

In terms of ICF simulations, two software packages are used in this paper, *Hydra* and *Cretin* [5]. *Hydra* is a multiphysics package in which the overall simulation is performed [8]. *Cretin* is the NLTE atomic physics package that calculates absorptivity and emissivity of elements which *Hydra* needs to perform the radiative transport calculations as part of the ICF simulation [9]. Despite *Hydra* being a simulation program consisting of a variety of physics calculations, *Cretin* often consumes seventy percent or more of the total computation time needed for ICF simulations. As a result, the fidelity and/or size of the simulations must be carefully balanced so as to fit within the time and resource constraints of the computer.

This is where machine learning, or more specifically neural networks, once again appears to be a great tool for improving performance via their simple evaluation and potential for parallel scalability. Past work has shown

that replacing the *Cretin* models with a set neural networks, consisting of a fully-connected autoencoder and a deep jointly informed neural network (DJINN) model, can produce significant (10x) speed-up in the atomic physics for a single element when used in conjunction with *Hydra* [5]. This use of an autoencoder and DJINN is analogous to reduced order modeling. The autoencoder, in this case, acts as a non-linear mapping to and from a low-dimensional space, and DJINN acts as a non-linear reduced order operator or solver on the low-dimensional space[10].

This paper demonstrates the extension of results of the *Cretin* surrogate model for different elements, but this paper is more specifically concerned with the ability to include multiple elements in a single neural network model for absorptivity or emissivity. Additionally, this paper will focus largely on the autoencoders. DJINN is, for the most part, an automatically constructed neural network, so there is little tuning to be done. That being said, the tuning of DJINN is not a concern in this paper. Also, the overall performance of the *Cretin* surrogate model is primarily dependent on the autoencoder’s performance. DJINN generally performs well and will learn the latent space of the autoencoder regardless of how well the autoencoder performs.

## 2. Related Work

This paper builds upon the work of Kluth, et al. [5]. The previous work utilized a fully-connected autoencoder which was trained to compress and decompress the spectra of krypton. Once trained, a DJINN model was trained to reproduce the latent space of the autoencoder using effectively the same input as *Cretin* : density, electron temperature, and a radiative field representation [11, 5]. The model as used in the implementation with *Hydra*

used an autoencoder to produce a compressed representation of the radiative field calculated by *Hydra*. The radiative field for the surrogate model used a weighted sum of a Planckian and a Gaussian distribution at a given radiation temperature and a specified m-band ratio. The weighting factor is the m-band ratio ( $\alpha$ ) where the m-band is a Gaussian distribution centered at 3 keV with a full width half maximum of 1 keV [5]. As implemented with *Hydra*, the neural network model was able to provide a speed-up of 10x over *Cretin* for just the atomic physics and a 7x speed-up for the overall simulation. This speed up was accompanied by less than one percent relative error for both the electron temperature and radiative temperature as compared to when *Hydra* uses data directly from *Cretin* [5].

### 3. Data

The data that was used to train the neural networks was generated by repeated execution of *Cretin* with different input parameters using steady state approximations. The inputs were uniformly sampled values for density, electron temperature, radiation temperature, and the m-band ratio. The m-band is a 2 keV - 4 keV emissivity band that can roughly approximate the radiative fields expected in an ICF experiment [12]. The absorptivity and emissivity are defined by the density, electron temperature, and the radiative field. For the purpose of generating radiative fields, the radiative field is further defined by radiative temperature and the m-band ratio using the function

$$I(\nu) = aT_r^4 [(1 - \alpha)b(\nu, T_r) + \alpha g(\nu)], \quad (1)$$

where,  $a$  is the radiative constant of  $7.5657 * 10^{-15}$  erg/cm<sup>3</sup>/K<sup>4</sup>,  $b(\nu, T_r)$  is the reduced Planckian, and  $g(\nu)$  is the previously mentioned Gaussian distribution centered at 3 keV with a full width half maximum set to 1 keV, and  $\alpha$  is the m-band ratio [5, 12]. This is the same as how data for krypton was generated in [5]. The ranges from which density, electron temperature, radiation temperature, and m-band ratio were sampled from were 0.003 g/cc to 0.1 g/cc, 300 eV to 3000 eV, 30 eV to 300 eV, and 0.0 to 0.3 respectively. Figure 1 shows two radiative fields generated in this manner. In this manner, 320,000 absorptivity spectra and 320,000 emissivity spectra with 200 logarithmically spaced energy bins were generated for beryllium, carbon, aluminum, iron, germanium, and krypton each. For clarification, one absorptivity spectra and one emissivity spectra were generated for each set of inputs.

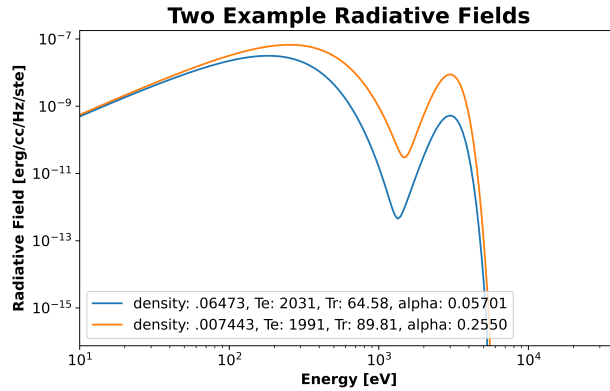


Figure 1: These are examples of two different radiative fields generated by the state process. The labels define the parameters used to generate the given radiative fields.

The elements were selected based on the desire to have a large range of atomic numbers (z numbers). This allowed the exploration a wide variety of spectra shapes. The authors also wanted the elements to be as relevant

to ICF experiments as possible, thus the authors chose beryllium, carbon, aluminum, iron, germanium, and krypton.

The way training and validation sets were handled was by giving each instance of a model its own 80/20 training/validation split which was randomly generated. The eighty percent for training was further split 90/10 training/validation at training time for the purpose of having validation cost versus epoch statistics. The spectral data was scaled differently depending on which architecture was used for the autoencoder. The two forms of scaling used were a cube root transform and a  $\log_{10}$  transform and were used either separately or in combination with each other. The  $\log_{10}$  transform used the equation  $x' = \log_{10}(x + 1)$ . Featurewise minmax scaling led to rather poor performance.

The data used to train the DJINN models consisted of the randomly sampled values used to generate the absorptivity spectra and emissivity spectra as inputs as well as the z-numbers of the elements. The resultant latent space of the associated autoencoders was used as the output.

#### 4. Training

One of the goals to demonstrate that the similar performance to the proof-of-concept could be achieved for elements other than krypton while also exploring how the performance changed with respect to the atomic number of the elements.

The architectures used in [5] were different depending on whether the autoencoder was trained on absorptivity spectra or emissivity spectra with them both being fully-connected neural autoencoders. The absorptivity architecture consisted of four hidden layers between the input layer and latent

Table 1: Summary of the proof-of-concept architectures.  $\log_{10}$  scaling was used for these models. The activation function used for all layers was the softplus function. Mean squared error was used as the cost function. [5]

	Absorption AE	Emission AE
Input dimension	200	200
Latent space dimension	5	7
Encoder	(96,46,22,10)	(124,77,48,29,18,11)
Total Parameters: Encoder + Decoder	50349	81287

space layer that had widths which were harmonically decaying down to the latent space of five. This layer-size pattern is then mirrored over the latent space layer to complete the autoencoder. In general the shape of autoencoders tend to resemble the shape of the network in Figure 2. The emissivity architecture consisted of six hidden layers between the input layer and latent space layers that had widths which were harmonically decaying down to the latent space of seven. Both architectures used the softplus function as the activation function for all layers. [5]. Table1 summarizes each of these architectures. Both of the architectures were trained using  $\log_{10}$  scaled spectra using a learning rate of 0.001 for 10,000 epochs with batch sizes consisting of 0.5% of the total training data set (the 80% fraction of the 320,000 spectra before the 90/10 split was applied). Adam was used as the optimizer, and mean square error was used as the cost function. The number of epochs, batch size, optimizer, and cost function stated here are used for all autoencoder models used in this paper.

A second goal was to determine whether a single, fully-connected architecture could be found that performed nearly as well or better than the proof-of-concept architectures while being smaller (use fewer parameters).

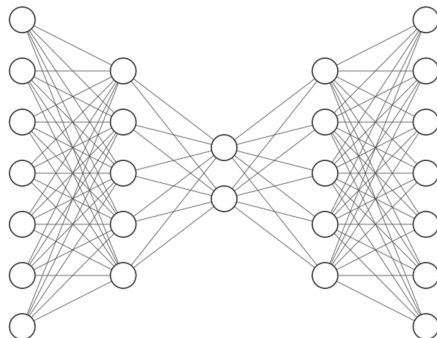


Figure 2: This is an example of a fully-connected autoencoder provided to demonstrate the hourglass shape seen in the majority of autoencoders. The latent space tends to be the smallest layer in the network. The left-hand side is the encoder, and the right-hand side is the decoder.

Table 2: Summary of the improved single-element architecture. Cube root scaling was used for this model. The activation function used for all layers was the softplus function. Mean squared error was used as the cost function.

Absorption and Emission AE	
Input dimension	200
Latent space dimension	10
Encoder	(100,33)
Total Parameters: Encoder + Decoder	47736

The architecture selected was found by using various layer width scalings such as division by constant factors (2,3,4,...) or factorial division (2 then 3 then 4...). The latent space was experimented with separately from the layer width scaling. Summarized in table 2, the improved architecture consists of only two hidden layers of widths 100 and 33 and a latent space dimension of 10. Like the proof-of-concept architectures, the activation function used was the softplus function. Some experimentation was done with the learning rate and scaling functions for the improved architecture, and it was decided

that the same learning rate would be used; however, the scaling function changed to a cube-root scaling function for reasons that will be explained in the results section.

Table 3: Summary of the multi-element architecture.

Absorption and Emission AE	
Input dimension	200
Latent space dimension	10
Encoder:	
Convolutional layer	1x5x20 stride: 1
FC layers	(100,50,30)
Total Parameters	818191
Encoder + Decoder	

The third and primary goal was to determine whether multiple elements could be placed in a single model. Early experiments demonstrated that a fully-connected model would not be particularly effective. As a result, a convolutional architecture was adopted which is summarized in table 3. The architecture used consisted of a convolutional layer that used twenty 1-by-5 filters which were applied with a stride of one. The convolutional layer was followed by fully-connected layers of widths of 100, 50, 30 with a latent space dimension of 10. The activation function used for all layers was the exponential linear unit (ELU). It should be noted that, in order to keep training time below twenty-four hours, only forty percent of the full data set of each element used in the convolutional network’s data set. More explicitly, this means that 128,000 spectra came from each element as opposed to 320,000 spectra for a total of 768,000 spectra.

To verify the viability of a multi-element model beyond that of just an



autoencoder a DJINN model was then trained to reproduce the latent spaces of each of the autoencoders. Figure 3 shows the general process of how the *Cretin* surrogate model is put together. The DJINN model uses densities, electron temperatures, radiation temperatures, m-band ratios, and z-numbers as the inputs, and it is trained to reproduce the latent space of the autoencoder, so the decoder can be used to map the latent space back to the full dimensions. For DJINN, in all cases, the initial learning rate is set to 0.001, the number of trees is 1, the maximum depth is 11, and drop-out is turned off. The DJINN models were trained for 1000 epochs with a batch size of 0.5% of the full size of the training data set.

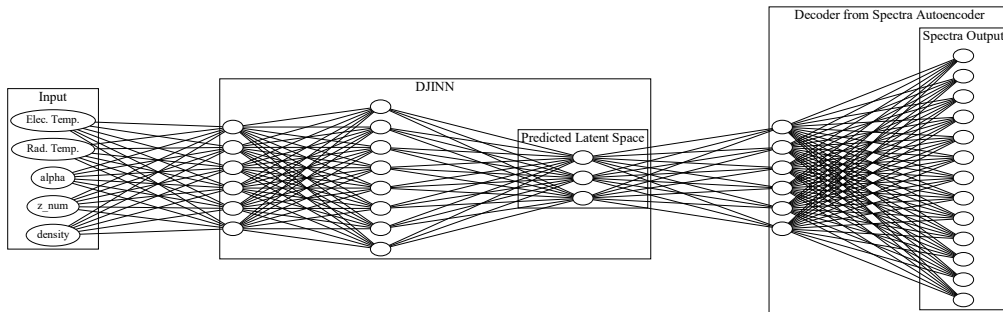


Figure 3: This neural network example graph demonstrates how the two different neural networks, DJINN and the decoder, are linked together. As used in this paper, these function as two individual networks that are trained separately.

## 5. Results

### 5.1. *Spectrum-integrate Autoencoder results*

Error results here are reported as percent relative error of a simple gray approximation of the spectra. A gray approximation is the summation or integral of either the absorptivity or emissivity over the energy range of the spectra. The two primary statistics of concern at this time are the mean

relative error and the maximum relative error of these gray approximations. The mean relative errors as reported are the arithmetic means of the mean percent relative error of five different models trained with the same architecture. The maximum relative error is the maximum percent relative error for any given spectra from any of five models having the same architecture. The errors are also reported after re-scaling back to the physical dimensions.

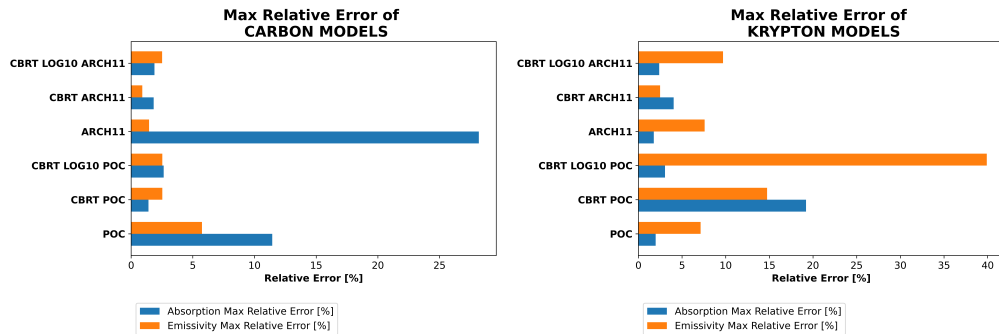


Figure 4: The maximum relative errors for the various single element models of carbon and krypton. ‘CBRT’ denotes the use of cube root scaling. LOG10 refers to the use of  $\log_{10}$  scaling. ‘CBRT LOG10’ references the use of cube root scaling followed by  $\log_{10}$  scaling. ‘POC’ denotes the proof-of-concept architecture, and ‘ARCH11’ denotes that the architecture selected was the eleventh architecture tested.

Figure 4 is provided to offer a look at what happens to the maximum relative error with the change of scaling functions. Here it can be seen that the maximum error for the  $\log_{10}$  scaled models exploded for the absorptivity of carbon. The “improved” krypton model does not have a better maximum error for absorptivity, but it does have better maximum error emissivity. The other elements actually displayed higher tendencies to perform better on the maximum error with the “improved architecture,” but the mean errors were a toss up between the cube root scaled “improved architecture” and the  $\log_{10}$  scaled proof-of-concept architecture. The performance on the low-z elements

Table 4: This table contains the mean percent relative error and maximum percent relative error of the multi-element model as well as the “improved” fully-connected (FC) model and the proof-of-concept (POC) model. The multi-element model consisted of iterations of the same model. The “improved” FC model and the POC model results are the results of the individual single-element models.

Absorptivity		Be	C	Al	Fe	Ge	Kr	All
Multi-element	mean	.181	.208	.231	.165	.176	.196	.211
	max	5.02	4.87	3.59	2.64	7.32	13.4	13.4
Improved FC	mean	.056	.365	.068	.137	.316	.087	-
	max	.882	1.83	3.23	2.46	2.82	4.04	-
POC	mean	.912	.473	.155	.094	.151	.149	-
	max	19.1	11.4	10.3	3.35	2.80	1.99	-
Emissivity		Be	C	Al	Fe	Ge	Kr	All
Multi-element	mean	.161	.238	.172	.215	.217	.189	.131
	max	4.24	4.77	5.73	1.97	1.62	12.5	12.5
Improved FC	mean	.167	.056	.119	.123	.109	.182	-
	max	.672	.905	5.87	2.42	3.10	2.49	-
POC	mean	.248	.589	1.53	.349	.560	.411	-
	max	3.12	5.74	50.0	11.3	15.3	7.13	-

ultimately decided which architecture was better. To answer questions about hyper-parameter tuning, experimentation occurred with the learning rate, but changing the learning rate to smaller values produced only slightly better mean relative errors with slightly worse maximum errors. This behavior is not entirely surprising because lower learning rates are often associated with worse generalization which often translates to higher maximum relative errors and sometimes lower mean relative errors [13].

Attempts to create a multi-element model were reasonably successful in that the model achieved an overall mean relative error 0.211% and 0.121%

for absorptivity and emissivity respectively, but the model is large, in terms of the number of parameters, than would be ideal considering the model has the approximately equivalent memory footprint of seventeen, fully-connected models. Attempts to make smaller multi-element models unsuccessful due to large mean relative errors and an increase in training time.

Table 4 more fully shows that the multi-element model performed comparably to the two different single-element model architectures on mean relative error for absorptivity and even beating the proof-of-concept mean error values for low- $z$  elements. The multi-element model also performed better than the proof-of-concept architecture for emissivity in mean error for each of the elements; however, the “improved” architecture tended to perform better for both absorptivity and emissivity on mean error. In terms of absorptivity maximum error, the multi-element model generally performed comparably with the “improved” architecture and beating the proof-of-concept model on the four lightest elements. The story is similar but not the same for the emissivity maximum error.

### *5.2. Spectral Performance of Autoencoders*

The plots in Figures 5 and 6 consist of the minimums, first quartiles, medians, means, third quartiles, and maximums of the bin-wise percent relative error averaged over each of the five iterations of the tested model. For example, the first quartiles are the average of the first quartiles over the five models. The average of the true spectra is then plotted on top of these to provide an idea of what spectral features may lead to increases in error. Thus, from Figures 5 and 6, a general idea of the uncertainty of the multi-element model can be obtained. Both the absorptivity and emissivity for both beryl-

lithium and krypton have a third-quartile that sticks very close to the median except at the highest of energy levels. Additionally, the third-quartiles of the emissivity errors stay below ten percent error until about 20 keV which is generally outside of the scope of ICF simulations. With the exception of the low- $z$  elements the absorptivity spectra have a rather flat level of error. While this does imply that a full quarter of the spectra produced errors even higher, those spectra still perform well below 0.1% relative error for the half or more of the full spectra. The equivalent plots for the single-element models, which are not shown here, possess increasing errors for the high energy portion of the spectra, but the maximum errors are not as large and cover. The point where the error starts climbing in the single-element models is delayed compared to the multi-element model. However, an issue with the single-element models is that they appear to be more prone to produce increased errors around sharp features in the spectra. This is opposed to the multi-element model, a convolutional model, being not immune but more resistant to such issues.

The majority of this increasing error is thought to be contributed by the increasingly small values. Also thought to contribute to the error is that neither the single-element models or the multi-element models are particularly great at reproducing highly non-linear curves which is particular issue for the emissivity spectra. The absorptivity spectra are rather linear if the absorption lines are neglected. The single-element model does seem to perform better on the emissivity as well because it should be better at capturing long range trends and thus the general shape of the data. This assumption is based on the idea that fully-connected models are effectively a large collection

of full dimension filters. The multi-element model, being convolutional, uses many small filters which likely makes it easier to reproduce sharp features but long range trends can be easily lost if the data is highly non-linear like with the emissivity spectra.

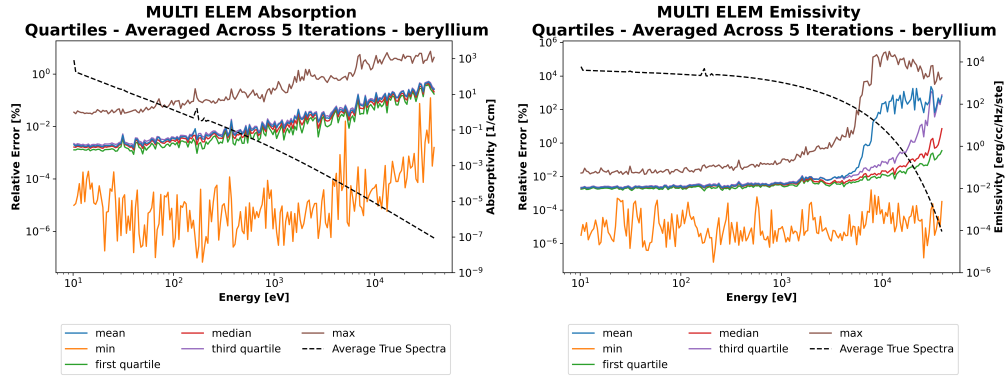


Figure 5: These plots show for the absorptivity and emissivity of beryllium the minimum, mean, maximum, quartiles, and the average spectra of the beryllium samples used. In the left plot it can be seen that the maximum error for absorptivity does exceed 1%. Also seen is that the middle quartiles are tightly clustered, but along with maximum error, the errors increase in a rather linear fashion as the energy goes up. The emissivity of beryllium, in the right plot, sees a large increase in maximum relative error around 10 keV which also results in a large increase in mean relative error. The middle quartiles do begin to diverge from each other around 20 keV.

To further explain why a cube root scaling, upon doing some investigating into why the low- $z$  elements did not perform as well as the high- $z$  elements for absorptivity without the cube root scaled models, it was found that there appeared to be some kind of threshold in the spectra at which all functionality was lost. It can be seen in Figure 7 that the ability of the neural networks to predict the values of the spectra breaks down at a threshold between  $10^{-3}$  and  $10^{-4}$ . This is likely due to the fact that our logarithmic scaling shifts the values by adding one. This shift makes the values of small, positive values indistinguishable from 0 (to the neural network's training). By using a cube

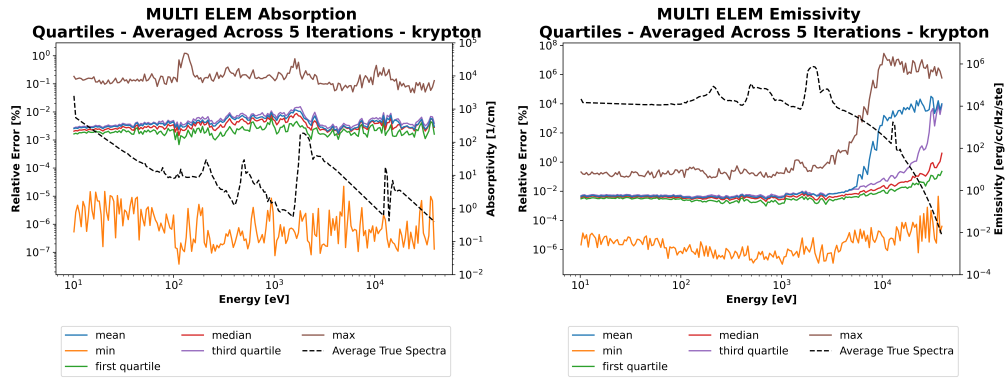


Figure 6: These plots show for the absorptivity and emissivity of krypton the minimum, mean, maximum, quartiles, and the average spectra of the krypton samples used. In the left plot it can be seen that the maximum error for absorptivity may just barely exceed 1%, but the performance is different from that of beryllium in that the maximum relative error is fairly stable across the entire energy range. Also, seen are that the middle quartiles are in close proximity to each other. Much like beryllium, krypton sees a large increase in maximum error for emissivity around 10 keV with a corresponding increase in mean error. The middle quartiles begin to diverge in a way that appears nearly identical to that of beryllium.

root function to scale, we recover a sensitivity to small, positive values of the data. Figure 8 indicates why this was only observed for low  $z$  elements: the magnitude and range of the emissivity and absorptivity are smaller in high  $z$  elements.

Figure 7 shows the results of what happens when  $\log_{10}$  scaling is used in a fully-connected autoencoder or samplewise minmax scaling is used in a convolutional autoencoder. There is rough threshold where values become too small and accuracy rapidly decreases. The spread between the spectra of the different elements seen in Figure 8 explains why this issue becomes less prevalent with increasing  $z$ -number especially for absorptivity.

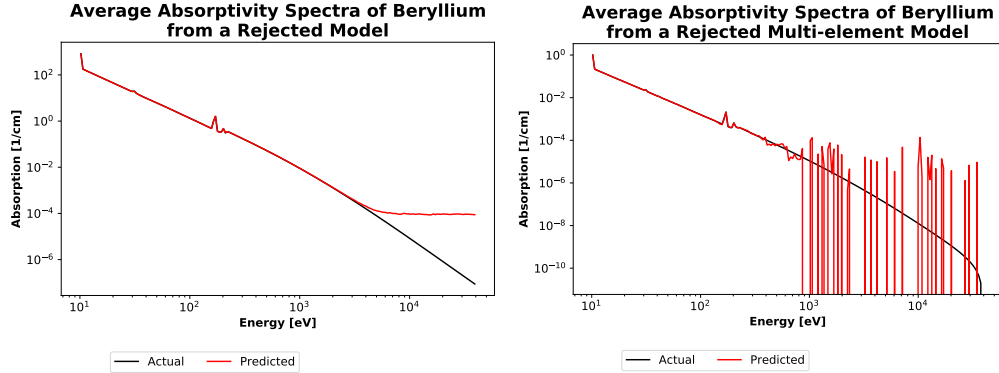


Figure 7: The issue that caused beryllium to have large error in its reproduction can occur in both a fully connected model or a convolutional model with multiple elements. The left model plot is from a model scaled with a  $\log_{10}$  scaling, and the right plot is from a the convolutional architecture used for multiple elements except with a samplewise minmax scaling. It can be seen here that once the values reach a certain small value the network ceased to reproduce them properly. This problem does not manifest with the cube root scaling.

### 5.3. Latent-space predictions using DJINN

After the selection of the “improved” and multi-elements architectures, DJINN models were trained with the models produced from them to see how they compare the performance of the proof-of-concept results. Figure 9 shows that the mean relative error of the multi-element models performs generally pretty well and reasonably close to the single-element models. The maximum relative error, though, does not show nearly the same performance. The DJINN model introduces enough noise that the maximum relative errors is generally multiplied by a factor between 10 and 100. The single-element models do not entirely show a clearly better model between the proof-of-concept and “improved” models. Figure 10 shows the maximum relative error of the single-element models. The emissivity of iron as reproduced with the POC autoencoder plus DJINN does very poorly, and it makes it



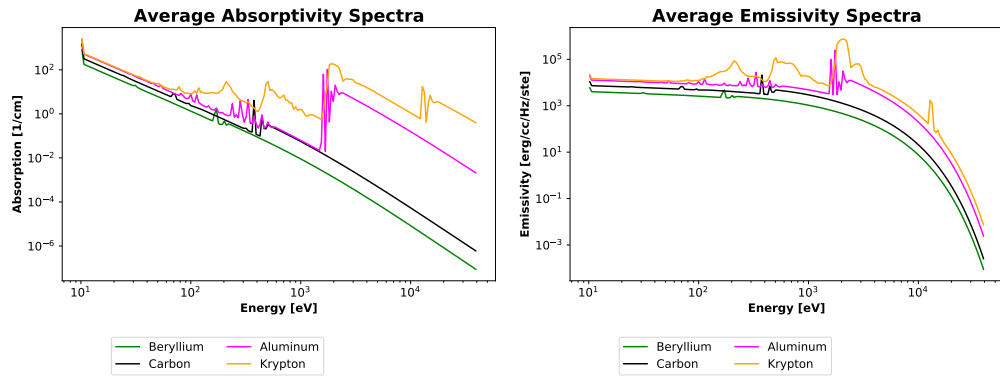


Figure 8: These are the average absorptivity and emissivity spectra for selected elements. Iron and germanium were not included to improve the readability of the plots.

difficult to tell that krypton and germanium tend to perform better with the model that uses the POC autoencoder. The mean relative error results which can be seen in Table 5 for the low-z elements point to the models that use the “improved” autoencoder being better which is similar to the maximum relative error, but the high-z elements tend to do a bit better with the models that use the POC autoencoder.

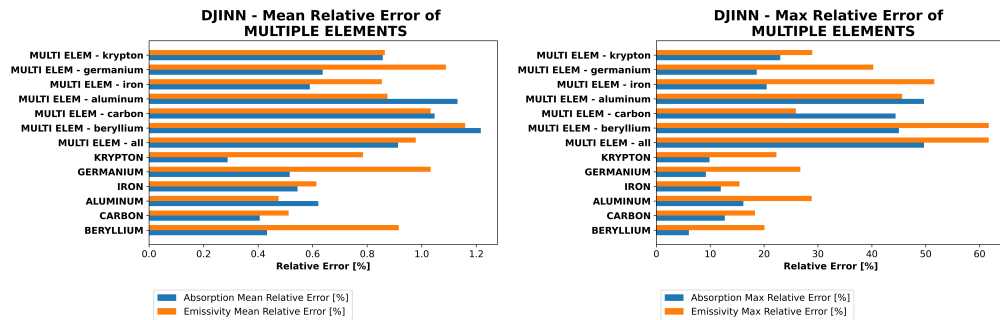


Figure 9: The maximum relative errors for the various single element models of carbon and krypton. All of these models used a cube-root scaling.

Table 5: This table contains the mean percent relative error and maximum percent relative error of the combined multi-element autoencoder and its associated DJINN model as well as the “improved” fully-connected (FC) model and the proof-of-concept (POC) model in combinations with their respective DJINN model. The multi-element model results all come from one convolutional model plus its associated DJINN model. The “improved” FC model and the POC model results are the those of the individual single-element models with each of them having its own DJINN model.

Absorptivity		Be	C	Al	Fe	Ge	Kr	All
Multi-element	mean	1.21	1.05	1.13	.590	.637	.857	.913
	max	45.0	44.4	49.7	20.5	18.6	23.0	49.7
Improved FC	mean	.433	.406	.621	.545	.516	.288	-
	max	6.04	12.7	16.2	12.0	9.19	9.88	-
POC	mean	.929	1.07	.391	.310	.497	.305	-
	max	28.5	17.7	12.7	12.2	32.4	8.42	-
Emissivity		Be	C	Al	Fe	Ge	Kr	All
Multi-element	mean	1.16	1.03	.875	.854	1.09	.865	.978
	max	61.7	25.9	45.6	51.6	40.3	29.0	61.7
Improved FC	mean	.916	.512	.475	.614	1.03	.785	-
	max	20.1	18.3	28.8	15.4	26.7	22.3	-
POC	mean	1.03	1.72	1.77	.741	.806	.791	-
	max	11.1	41.2	55.0	264	15.9	13.0	-

## 6. Conclusion and Future Work

It has been shown here that the previous work done in the proof-of-concept [5] can be reproduced for various other elements. In this process it was discovered that low-z elements or rather that low values of absorptivity and emissivity are not able to be reproduced accurately under the scaling methods used in the proof-of-concept. In place of the  $\log_{10}$  scaling that was previously used, cube root scaling is now being used which compresses the magnitudes of the spectra in a manner that reduces reliance on high-precision

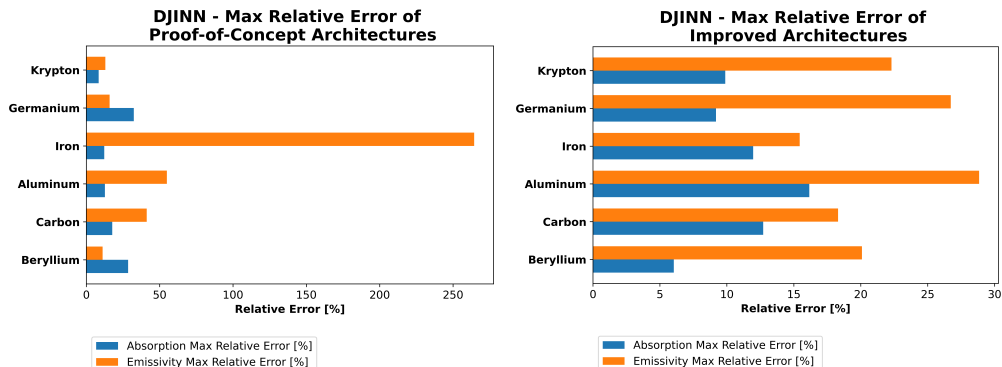


Figure 10: The maximum relative errors for the various single element models of carbon and krypton. ‘CBRT’ denotes the use of cube root scaling. LOG10 refers to the use of  $\log_{10}$  scaling. ‘CBRT LOG10’ references the use of cube root scaling followed by  $\log_{10}$  scaling. ‘POC’ denotes the proof-of-concept architecture, and ‘ARCH11’ denotes that the architecture selected was the eleventh architecture tested.

calculations. Then, by using a convolutional autoencoder was effectively employed to encode and decode the absorptivity and emissivity spectra of multiple elements in a single model but not with the same accuracy as the single-element models. Lastly, it was demonstrated that DJINN, with the inclusion of the elements’ z-numbers as inputs, managed to learn the latent space of the decoder of the multi-element model, but with significantly more uncertainty than the single element models.

Directly continuing from this work will include better tuning of the DJINN model, so the multi-element model may obtain performance far closer to that demonstrated by the single-element models. This process will also likely include the implementation of transfer learning in the sense of linking multiple pretrained models end to end and proceeding to train it further.

Benefiting from the attempts to improve the multi-element model performance will be the *Hydra* simulations in which the multi-element model will be used to replace *Cretin*. Preliminary maximum relative error results

suggest that plenty of tuning will be needed, but mean relative error are still reasonably low.

Lastly, further work will be done on the autoencoder to decrease the memory footprint. There may be additional experimentation with less commonly used architectures in a search to find a model that is more accurate, has a smaller footprint, or possesses both qualities. Other efforts may include changing what kind of loss function is used, further experimentation with the scaling functions, as well as some different training processes to introduce sparsity.

## **Acknowledgements**

This work was performed under the auspices of the U.S. Department of Energy by Lawrence Livermore National Laboratory under Contract DE-AC52-07NA27344. Released as LLNL-JRNL-822718-DRAFT.

This document was prepared as an account of work sponsored by an agency of the United States government. Neither the United States government nor Lawrence Livermore National Security, LLC, nor any of their employees makes any warranty, expressed or implied, or assumes any legal liability or responsibility for the accuracy, completeness, or usefulness of any information, apparatus, product, or process disclosed, or represents that its use would not infringe privately owned rights. Reference herein to any specific commercial product, process, or service by trade name, trademark, manufacturer, or otherwise does not necessarily constitute or imply its endorsement, recommendation, or favoring by the United States government or Lawrence Livermore National Security, LLC. The views and opinions of authors expressed herein do not necessarily state or reflect those of the United

States government or Lawrence Livermore National Security, LLC, and shall not be used for advertising or product endorsement purposes.

A thank you goes to Gilles Kluth for help in running *Cretin* as well as providing the krypton data.

## References

- [1] T. Gilliam, T. Jones, G. Chapman, J. Cleese, E. Idle, M. Palin, Monty Python and the Holy Grail, Michael White Productions, 1975.
- [2] M. Claessens, Quest for the Holy Grail of Fusion, Springer International Publishing, 2020, pp. 189–198.
- [3] J. Kline, et al., Progress of indirect drive inertial confinement fusion in the united states, Nuclear Fusion 59 (2019). doi:<https://doi.org/10.1088/1741-4326/ab1ecf>.
- [4] D. Salzmann, Atomic Physics in Hot Plasmas, EBSCO ebook academic collection, Oxford University Press, 1998.  
URL <https://books.google.com/books?id=PI7mCwAAQBAJ>
- [5] G. Kluth, K. Humbird, B. K. Spears, J. L. Peterson, H. A. Scott, M. V. Patel, J. Koning, M. Marinak, L. Divol, C. V. Young, Deep learning for nlte spectral opacities, Physics of Plasmas 10 (2020). doi:<https://doi.org/10.1063/5.0006784>.
- [6] D. A. Holladay, C. J. Fontes, W. P. Even, R. G. McClarren, An accelerated approach to inline non-lte modeling, High Energy Density Physics 34 (2020) 100746.

- [7] D. A. Holladay, Studying effects of non-equilibrium radiative transfer via hpc, Ph.D. thesis, Texas A&M University (May 2018).
- [8] M. M. Marinak, G. D. Kerbel, N. A. Gentile, O. Jones, D. Munro, S. Pol-laine, T. R. Dittrich, S. W. Haan, Three-dimensional hydra simulations of national ignition facility targets, *Physics of Plasmas* 8 (5) (2001). doi:<https://doi.org/10.1063/1.1356740>.
- [9] H. A. Scott, Cretin - a radiative transfer capability for laboratory plas-mas, *Journal of Quantitative Spectroscopy & Radiative Transfer* 71 (2001).
- [10] K. Lee, K. T. Carlberg, Model reduction of dynamical systems on non-linear manifolds using deep convolutional autoencoders, *Journal of Com-putational Physics* 404 (2020). doi:<https://doi.org/10.1016/j.jcp.2019.108973>.
- [11] K. D. Humbird, J. L. Peterson, R. G. McClarren, Deep neural network initialization with decision trees, *IEEE Transactions On Neural Net-works and Learning Systems* 30 (5) (2019).
- [12] Y. Li, W. Huo, K. Lan, A novel method determining the m-band fraction in laser-driven gold hohlraums, *Physics of Plasmas* 18 (2011).
- [13] Y. Li, C. Wei, T. Ma, Towards explaining the regularization effect of initial large learning rate in training neural networks, 33rd Conference on Neural Information Processing Systems (NeurIPS 2019) (2019).